THE JOURNAL OF PHYSICAL CHEMISTRY C
A JOURNAL OF THE AMERICAN CHEMICAL SOCIETY

pubs.acs.org/JPCC Article

Composition-Dependent Formation and Dissociation of Structure I and Structure II Clathrate Hydrates of Trimethylene Oxide in Ultrahigh Vacuum

Soham Chowdhury, Bijesh K. Malla, Gaurav Vishwakarma, Anupriya Nyayban, and Thalappil Pradeep*

Cite This: *J. Phys. Chem. C* 2025, 129, 8937−8945 Read Online

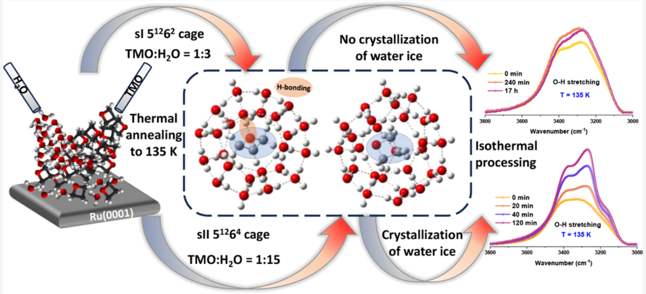

ABSTRACT: This study reports the formation of structure I (sI) and structure II (sII) clathrate hydrates (CHs) of trimethylene oxide (TMO) at different concentrations of the components under cryogenic conditions in ultrahigh vacuum. We codeposited TMO:H_2O ices of 1:3 and 1:15 ratios at 10 K and thermally annealed them to 135 K. Using reflection−absorption infrared spectroscopy, we observed the formation of distinct CH structures from compositionally varied ices at 135 K. Although TMO occupied the $5^{12}6^2$ cage of sI CH in the 1:3 mixture, in the 1:15 mixture, it occupied the $5^{12}6^4$ cage of sII. The sI TMO CH demonstrated greater thermal stability compared to sII. Interestingly, the dissociation of these CH structures exerts different effects on amorphous solid water (ASW). While the sI CH dissociation does not lead to the expected conversion of ASW to crystalline hexagonal ice, the dissociation of sII CH crystallizes ASW. This observation may be attributed to the relative stability and host−guest hydrogen bonding of the CHs, as supported by density functional theory analysis.

INTRODUCTION

Formation of clathrate hydrates (CHs) in laboratory interstellar conditions has been established by several studies using reflection−absorption infrared spectroscopy (RAIRS).[1−5] Subsequently, Tychengulova et al. have reported infrared spectroscopic investigations of the formation of CO_2 CH under simulated interstellar environments.[6] Besides RAIRS, a recent study has shown the formation of tetrahydrofuran and 1,3-dioxolane under ultrahigh vacuum (UHV) and cryogenic conditions by reflection high-energy electron diffraction (RHEED).[7] The chemically diverse interstellar medium (ISM) contains more than 300 species, such as neutral atoms and molecules, cations, anions, and radicals.[8] These species exist in the gas phase or in the solid phase on interstellar ice-dust.[9,10] As the ice matrices are predominantly rich in water, many molecular species may be entrapped in them as CHs, forming different structures. The size of the CH cages depends on the size of the guest molecule, which determines whether the CH will be in structure I (sI) or structure II (sII) or structure H (sH).[11] Temperature and pressure are two crucial parameters to decide the CH structure for a particular guest molecule. Additionally, one structure can be converted to another, either by altering the condition or by introducing other foreign molecules.[12,13] Most of these studies have been conducted under high-pressure conditions, where the guest molecule is forced to occupy the hydrate cage. However, in UHV, this mechanism is different, particularly for nanoscale thin film ices, at cryogenic temperatures. Here, thermal annealing of the mixed ice containing host and guest molecules enables their mobilization, followed by reorientation of the water molecules, resulting in enclathration of the guest, all under UHV.[14]

Trimethylene oxide (TMO), a four-membered cyclic ether, has yet to be detected in space. However, recently its structural isomer, propylene oxide, has been detected in ISM.[15] Ethers are known to form CH; for example, tetrahydrofuran, a five-membered cyclic ether, and dimethyl ether, a noncyclic ether, form $5^{12}6^4$ cages of sII CH in UHV.[3,16] Ethylene oxide, a three-membered cyclic ether analogous to TMO, commonly forms $5^{12}6^2$ cage of sI CH in atmospheric pressure and in vacuum.[17,18] The CH structure and its cage size are largely dictated by the size and chemical nature of the guest molecule. TMO has an intermediate size between ethylene oxide and tetrahydrofuran. Investigating TMO CH structure under UHV is crucial for understanding how molecules behave in a water ice matrix and occupy clathrate cages at cryogenic temperatures (10−135 K).

Received: March 10, 2025
Revised: April 21, 2025
Accepted: April 23, 2025
Published: May 5, 2025

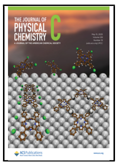

https://doi.org/10.1021/acs.jpcc.5c01603

There are a few reports on the effect of composition in TMO CH formation, where CHs are formed by vapor deposition of guest molecules on crystalline ice nanocrystals.[19−22] However, there is no such study of the formation of TMO CH in amorphous ice under UHV. Also, the consequence of their dissociation affecting the crystallization of ice has hitherto not been observed. The effect of CH dissociation on the crystallization kinetics of amorphous solid water (ASW) provides new insights into the physical transformations of icy bodies in space. Deciphering how guest molecules interact with ASW and contribute to phase transitions enhances our understanding of the stability and structural evolution of materials in extraterrestrial environments.

Here, we report the formation of TMO CHs from amorphous TMO-H_2O mixed ice by thermally annealing the mixtures from 10 to 135 K. We observed the formation of sI and sII CH from 1:3 and 1:15 mixtures of TMO and H_2O, respectively, under identical temperature and pressure conditions. For the first time, we demonstrate the role of composition in CH formation under UHV conditions. The RAIR spectra illustrate the formation of two CHs using two vibrational modes: for sI using the ring puckering mode and for sII using the C−O−C stretching mode. These observations are supported by density functional theory (DFT) analyses, which highlight the influence of host−guest hydrogen bonding and a distorted planar geometry of TMO in the CHs. Interestingly, the dissociation of these two types of CH structures impacts the ASW differently. While the dissociation of sII CH crystallizes ASW into hexagonal ice at 135 K, as expected, the dissociation of sI CH does not induce this phase transition, leaving the amorphous ice intact. This contrasting effect is attributed to the greater stability of sI compared to sII, as evidenced by the RAIR study as well as the DFT analyses.

■ EXPERIMENTAL SECTION

All experiments were conducted using a UHV chamber maintained at a base pressure of ∼5×10^{-10} mbar, illustrated in Figure 1. The apparatus is described in detail elsewhere.[23−25] Briefly, the chamber is equipped with several analytical techniques, including RAIRS, low-energy ion scattering (LEIS), mass spectrometry, secondary ion mass spectrometry (SIMS), temperature-programmed desorption mass spectrometry (TPD-MS), and a vacuum ultraviolet deuterium continuum source. The base pressure of the vacuum chamber is achieved by six turbomolecular pumps, further supported by scroll pumps. A single-crystal Ru(0001) substrate of 1.5 cm in diameter and 1 mm in thickness was used for our experiments to grow nanoscale ice films. This substrate was mounted on a copper holder and placed at the tip of a closed-cycle helium cryostat. The substrate is also equipped with a 25 Ω resistive heater, allowing precise temperature control in the range of 8 to 1000 K. Temperature measurement was achieved using a platinum sensor and a K-type thermocouple, providing a temperature accuracy of 0.5 K. Before each experiment, the Ru(0001) was heated to 400 K repeatedly to ensure cleanliness. It is worth noting that the substrate has no effect in this study due to multilayer deposition.

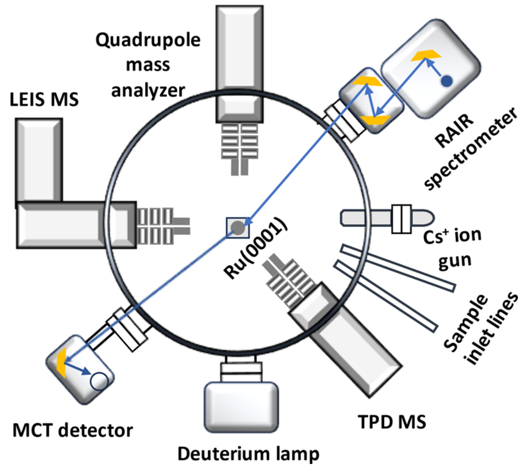

Figure 1. Schematic diagram of the experimental setup. As shown in this representation, the Ru(0001) substrate is oriented to perform the RAIR experiment.

Milli-Q water (H_2O of 18.2 MΩ resistivity) and TMO (99.9%, Sigma-Aldrich) were taken in two separate vacuum-sealed test tubes (with a glass-to-metal seal) and were further purified by several freeze−pump−thaw cycles. TMO and H_2O were connected to the UHV chamber through separate sample inlet lines. Precise control over the deposition of these two samples was achieved by utilizing all-metal leak valves. For quantification purposes, we considered that 1.33×10^{-6} mbar exposure for one second, equated to 1 monolayer (ML), was estimated to contain approximately 1.1×10^{15} molecules cm^{-2}, assuming an ion gauge sensitivity factor of unity.[26] The ion gauge sensitivity factor of H_2O is ∼1.0, and for TMO, it is considered as ∼3.0 based on the known sensitivity factor for tetrahydrofuran (THF), chemically similar cyclic ether.[27] To deposit 300 ML of ice consisting of a 1:3 ratio of TMO and H_2O mixture, the chamber was backfilled to a total pressure of 5×10^{-7} mbar for 10 min with TMO reaching 2.5×10^{-7} mbar and the H_2O pressure maintained at 2.5×10^{-7} mbar. The other two ratios of TMO and H_2O (1:15 and 1:30) were prepared at 10 K by keeping the total pressure constant and changing the inlet pressure of TMO and H_2O accordingly. During codeposition, the total chamber pressure typically varies between 4.90×10^{-7} and 5.10×10^{-7} mbar, resulting in a variation of approximately 10−15 ML in total thickness for a 300 ML ice film. For instance, a 1:3 TMO:H_2O mixture is achieved by maintaining the partial pressure of each component at ∼2.50×10^{-7} mbar (due to the difference in gauge sensitivity factors). The maximum fluctuation in individual partial pressure is around 0.10×10^{-7} mbar, which translates to ∼5−8 ML variation per component in a 300 ML film. As a result, the composition of 1:3 mixed ice can be varied from 1.11:3 to 0.89:3 and from 1:3.11 to 1:2.89. This gives an uncertainty of ±0.11 in the mixing ratio for the 1:3 ice. Throughout the vapor deposition process, mass spectra were continuously obtained to verify both the purity and the ratio of the deposited molecules.

The formation and dissociation of TMO CH were investigated using RAIR spectroscopy. RAIR spectra were recorded in the 4000−550 cm^{-1} range with a spectral resolution of 2 cm^{-1}, using a Bruker Vertex 70 FT-IR spectrometer equipped with a liquid-nitrogen-cooled mercury cadmium telluride (MCT) detector. The IR beam path outside the UHV chamber was continuously purged with dry nitrogen to avoid absorption from atmospheric gases.

Computational Details. All of the electronic structure calculations were performed using the Gaussian 09 software package. At first, the ground-state geometries of the TMO and

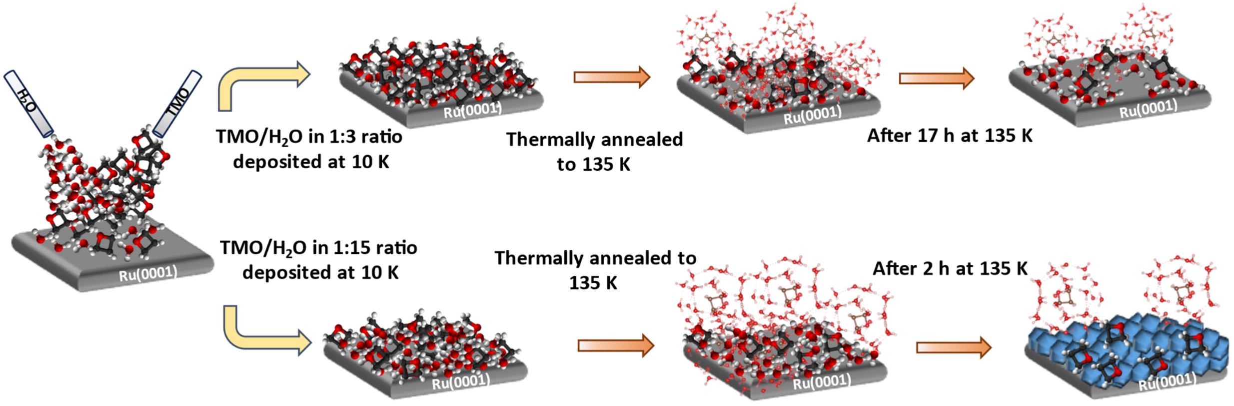

Figure 2. Schematic illustration of TMO CH formation in water ice at 135 K. The vapors of TMO and H_2O were deposited at 1:3 and 1:15 ratios, respectively, and thermally annealed to 135 K. The blue three-dimensional film represents hexagonal water ice.

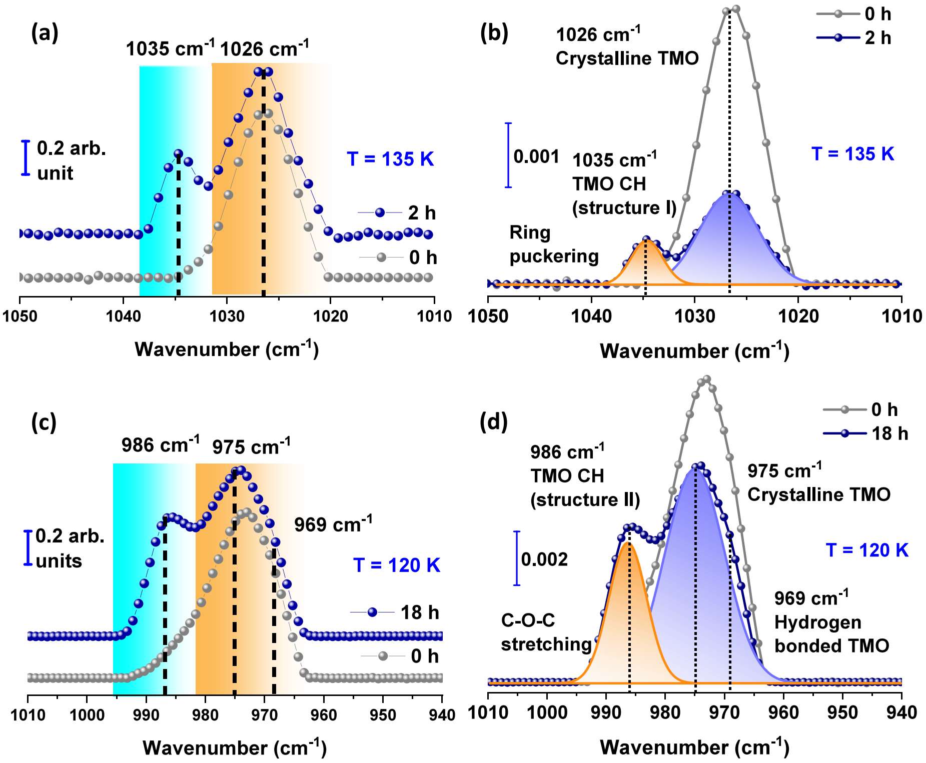

Figure 3. RAIRS study of sI and sII CH of TMO in two spectral regions. (a, b) Time-dependent RAIR spectra of 300 ML of TMO-H_2O of 1:3 composition at 135 K in the ring puckering mode region. (a) Normalized and (b) deconvoluted spectra. (c, d) Time-dependent RAIR spectra of 300 ML of TMO-H_2O of 1:15 composition at 120 K in the C−O−C stretching region. (c) Normalized and (d) deconvoluted spectra. In parts b and d, the intensity loss at 2 and 18 h, respectively, is due to desorption in UHV.

the CH cages (namely, the 5^{12}, $5^{12}6^2$, and $5^{12}6^4$ cages) were optimized using DFT at the B3LYP/6-311++g(d,p) level of theory. Next, the optimized TMO molecule was placed inside the optimized CH cages, and the geometries were reoptimized at the same level of theory. Furthermore, frequency calculations are performed to justify that these geometries are at the minimum of the potential energy surface, and these calculations generate nonimaginary frequencies, confirming that these geometries are in the ground state. The binding energies of sI and sII CHs were obtained by subtracting the ground state energy of optimized TMO and empty CH cages from the optimized TMO CH structures. The dihedral angle of TMO inside $5^{12}6^2$ and $5^{12}6^4$ cages was calculated, and host−guest hydrogen bonding was identified from DFT-optimized CHs.

■ RESULTS AND DISCUSSION

TMO CHs were prepared by thermally annealing codeposited ice mixtures of TMO and H_2O at two varying compositions (Figure 2). After TMO and H_2O were deposited at 10 K for 300 ML of thickness, the samples were slowly heated to 135 K at a heating rate of 5 K min^{-1}, followed by isothermal processing of ice for an extended period. The experiments were carried out at different compositions of the TMO and H_2O ice. In one experiment, TMO and H_2O mixed ice were created at a 1:3 composition, and in another mixed ice, TMO and H_2O were taken at a 1:15 composition.

The RAIR spectrum of 150 ML pure TMO in the ring puckering region is plotted in Figure S1b, showing the 1026 cm^{-1} peak attributed to this mode of crystalline TMO. The TMO-H_2O ice mixture at 135 K for 1:3 composition presents this peak at 0 h in Figure 3a,b. However, upon annealing for 2 h at 135 K, a new peak emerges at 1035 cm^{-1}, indicating a structural change. This peak is attributed to TMO in the large $5^{12}6^{2}$ cage of sI CH, consistent with the findings by Buch et al. and others.[19−21] The RAIR spectrum was further deconvoluted to assign the crystalline and CH phases of TMO in Figure 3b, and the relative percentages of CH and crystalline fractions of TMO were estimated as 20.72 and 79.28%, respectively.

In a similar manner, the 1:15 ice composite was thermally annealed at 120 K. The RAIR spectra in the C−O−C stretching shown in Figure 3c,d exhibit a peak at 975 cm^{-1}. A comparison with the spectrum of 150 ML TMO in the C−O−C stretching region (Figure S1a) confirms that the peak at 975 cm^{-1} is characteristic of crystalline TMO. After 18 h at 120 K, a new peak appears at 986 cm^{-1} alongside the crystalline TMO feature. This new peak is assigned to TMO in the large $5^{12}6^{4}$ cage of sII CH.[19−21] Also, a small quantity of TMO forms hydrogen bonds between the hydrogen of H_2O and the ethereal oxygen of TMO, resulting in a red-shifted peak at 969 cm^{-1}, in the C−O−C stretching region.[28] Deconvolution of the RAIR spectrum is shown in Figure 3d, and the relative percentages of CH, crystalline TMO, and hydrogen-bonded TMO are 27.77, 66.98, and 5.25%, respectively.

The C−O−C stretching region of 1:3 composition is plotted in Figure S2a. Here, the sI CH feature is assigned. The deconvoluted spectrum of 1:3 composition in C−O−C stretching reveals peaks at 975, 981, and 989 cm^{-1}. As attributed above, the peak at 975 cm^{-1} corresponds to the crystalline TMO (shown in Figure 3d), whereas the other two blue-shifted peaks indicate the confined state of the TMO in water ice. Ethers are known to form clusters. As Fleyfel et al. suggested, TMO may form clusters in water ice at higher concentrations.[20] The peak at 981 cm^{-1} corresponds to the TMO cluster, while the peak at 989 cm^{-1} is attributed to the $5^{12}6^{2}$ cage of sI, as its position is 3 cm^{-1} higher than the 986 cm^{-1} peak, associated with sII CH. This is expected for the smaller $5^{12}6^{2}$ cage of sI, where TMO experiences more confinement than the larger $5^{12}6^{4}$ cage of sII. The 969 cm^{-1} peak is not observed in the C−O−C stretching of sI CH (Figure S2a). This is because, in a 1:3 ratio, crystalline TMO resides as isolated TMO clusters in ASW. This structural change prevents further interaction between TMO and free water molecules, as evidenced by the absence of the hydrogen-bonded feature (969 cm^{-1}).

Additionally, the ring puckering region of the 1:15 composition plotted in Figure S2b also confirms the presence of sII CH. The 1030 cm^{-1} feature of larger sII CH is 5 cm^{-1} red-shifted than the 1035 cm^{-1} peak of smaller sI CH. The peak at 1026 cm^{-1} is due to crystalline TMO.

We further investigated whether codeposition is a prerequisite for composition-dependent CH formation or if sequential deposition at the same composition would also lead to sI and sII CH. Figures S3 and S4 illustrate this with the formation of CH in sequentially deposited TMO and H_2O ice in 1:3 and 1:15 ratios, respectively, followed by thermal annealing from 10 to 140 K. The temperature-dependent spectra in Figure S3 show that the 1035 cm^{-1} peak emerges at 130 K in 1:3 TMO-H_2O layered ice, confirming the formation of sI CH, whereas the 986 cm^{-1} peak appears in 1:15 TMO-H_2O layered ice, confirming the formation of sII CH (Figure S4).

To understand the effect of composition, the TMO-H_2O mixed ices were prepared at various compositions and isothermally processed at elevated temperatures (Figure S5). Figure S5a,b show that sI CHs are formed at ratios of 2:3 and 5:3 at 135 K, featuring the 1035 cm^{-1} peak. Similarly, the 986 cm^{-1} peak emerges in 1:6 and 1:30 compositions of mixed ices, due to sII CH. Combining the results of Figures 3 and S5, the trend in these compositions is stated as follows. The sI CH is formed at 5:3, 2:3, and 1:3 ratios, whereas the sII CH is formed at 1:6, 1:15, and 1:30 ratios. Here, 1:3 is the limiting composition, as equal or more concentration of TMO than H_2O in mixed ice leads to sI. If the concentration of TMO is slightly less than H_2O in mixed ice, it always leads to sII for all the compositions, ranging from 1:6 to 1:30.

To support our IR results of the formation of large $5^{12}6^{2}$ and $5^{12}6^{4}$ cages of sI and sII, we conducted quantum chemical calculations of TMO within these CH cages. The calculations allowed us to compute the infrared frequencies of their vibrational modes. Our calculations reveal a significant shift in the vibrational frequencies between the optimized structures of free TMO and TMO encaged in CH. Figure 4 illustrates the optimized structures of TMO within 5^{12},$5^{12}6^{2}$, and $5^{12}6^{4}$ cages. The optimized structure of TMO (Figure 4a) was unstable within the smaller 5^{12} cage (Figure 4b).[29] Higher molecular size with respect to the small cage size leads to instability and cage rapturing. However, in the case of $5^{12}6^{2}$ and $5^{12}6^{4}$ cages (Figure 4c,e), the TMO was stable. These results are justifiable as the molecular diameter of TMO across the C−O axis is 6.1 Å, and therefore, it could not be accommodated in a smaller 5^{12} cage, which has a cavity diameter of 5.09 Å. The cavity diameter of the sI $5^{12}6^{2}$ cage is 5.86 Å, slightly smaller than the size of TMO. The $5^{12}6^{4}$ cage of sII with 6.6 Å as the cavity diameter, is much larger in size than TMO.[22,30] As a result,

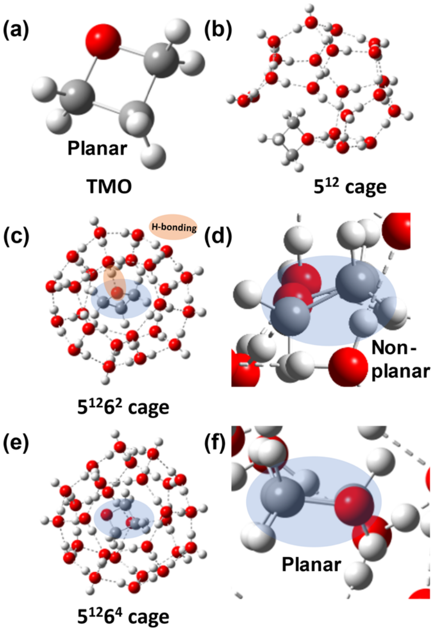

Figure 4. DFT-optimized structures of TMO trapped within various CH cages. (a) Free TMO compared with (b) 5^{12}, (c) $5^{12}6^{2}$, (d) $5^{12}6^{2}$ zoomed in, (e) $5^{12}6^{4}$, and (f) $5^{12}6^{4}$ zoomed in structures. Color codes used: white, H; red, O; and gray, C.

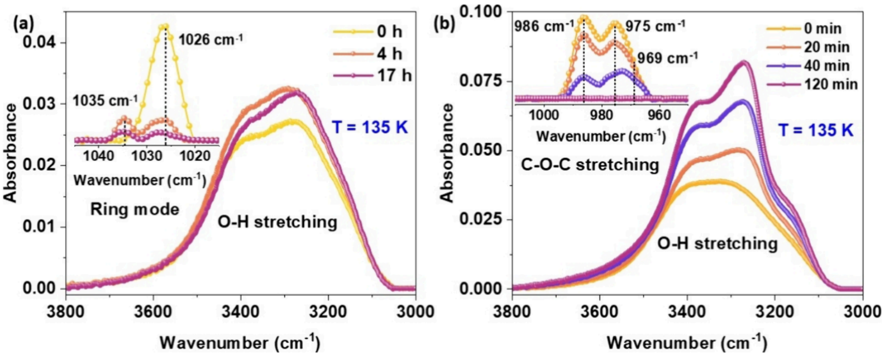

Figure 5. (a) Time-dependent RAIR spectra of 300 ML of a TMO-H_2O ice mixture (1:3) at 135 K in the O−H stretching region. The corresponding RAIR spectra in the ring mode region are shown in the inset. (b) Time-dependent RAIR spectra of 300 ML of a TMO-H_2O ice mixture (1:15) at 135 K in the O−H stretching region. The corresponding RAIR spectra in the C−O−C stretching region are shown in the inset.

TMO is constricted in the $5^{12}6^2$ cage and forces the cage to expand slightly.

The binding energies of TMO CHs are calculated by subtracting the energy of the optimized empty cage + the optimized free TMO from the energy of the optimized TMO CHs. It shows that the binding energy of sI (−2.18 eV) is more negative than that of sII (−2.07 eV), implying the greater stability of sI than sII (Table S2). The DFT-optimized structure depicts the host−guest hydrogen bonding between TMO and H_2O in sI CH, reaffirming the proximity of TMO and H_2O in the $5^{12}6^2$ cages (Figure 4c). Possibly due to hydrogen bonding as well as the steric hindrance in a tightly fitted $5^{12}6^2$ cage, this planar cyclic ether molecule gets distorted and becomes nonplanar (Figure 4d). The dihedral angle of trapped TMO is calculated from the optimized CH structures. The result shows that the dihedral angle of TMO is 9.2° and 1.3° in the $5^{12}6^2$ and $5^{12}6^4$ cages, respectively (Table S2). This implies a distorted nonplanar structure of TMO in the $5^{12}6^2$ cage, which can be attributed to the distortion caused by TMO-H_2O hydrogen bonding. This hydrogen bonding is absent in sII, and TMO remains almost planar (Figure 4f), with a limited deviation from its original structure.

These DFT-optimized structures suggest the reason for identifying the two CHs in two different vibrational modes. The C−O−C stretching mode manifests CH formation in sII, as observed for cyclic ether CHs.[31,32] This is not observed in sI, where the ring puckering mode manifests CH formation. The ring puckering mode is less active for the planar structure and more active for the distorted planar structure. Therefore, in sI, the distorted TMO activates the ring puckering mode strongly, and CH formation is evident in it. In sII, the ring puckering mode is less active, and as a result, the C−O−C stretching mode prominently manifests the CH formation.

Results of theoretical calculations of vibrational frequencies of free TMO and TMO trapped in the ring puckering mode of $5^{12}6^2$ and the C−O−C stretching mode of $5^{12}6^4$ cages are presented in Table S1. The experimental blue-shift for TMO CH is compared theoretical blue-shift. As it is encaged, the steric hindrance hardens the frequencies. A blueshift of 12 cm^{-1} was observed for TMO within the $5^{12}6^2$ cage (ring puckering mode), while a blueshift of 10 cm^{-1} occurred in the $5^{12}6^4$ cage (C−O−C stretching mode). Experimentally, we observed that the crystalline TMO shows peaks at 1026 and 975 cm^{-1} due to ring mode and C−O−C stretching mode, respectively, which shift to 1035 and 986 cm^{-1} with an increase of 9 and 11 cm^{-1}, respectively. It has been reported that the $5^{12}6^2$ cage expands slightly to accommodate the TMO, which may cause this difference in theoretical and experimental observations. Overall, the theoretically calculated positions match well with the experimental data for both $5^{12}6^2$ and $5^{12}6^4$ cages and, thereby, ascertain the formation of sI and sII structures.

The dissociation of metastable CHs leading to the crystallization of ASW is observed in UHV for several CHs as a generic physical phenomenon at cryogenic temperatures.[33,34] During the formation of CH, the amorphous water ice becomes more structurally ordered. As CH dissociates at a higher temperature, the desorption of the enclathrated guest molecule mobilizes the water molecules in the vicinity of the cage, promoting rapid reorientation. This facilitates the conversion of amorphous ice into either hexagonal or cubic ice.[33−35] This phenomenon was particularly evident in the dissociation of sII CH of TMO. It dissociates completely at 135 K within 2 h, and simultaneously, amorphous water was converted to hexagonal ice, as shown in Figure 5b. As dissociation progresses, the broad peak in the O−H stretching region becomes narrower and sharper with time. This continuous transformation in the IR spectra reflects the gradual conversion of amorphous water ice to crystalline ice. Despite this crystallization, water does not desorb from the matrix at 135 K, maintaining a constant concentration. As shown in the inset, the IR peaks at 986, 975, and 969 cm^{-1} decrease rapidly, as shown in the C−O−C stretching region (Figure 5b). This indicates that TMO, previously confined within the CH cages, is desorbed from the ice matrix along with crystalline TMO and hydrogen-bonded TMO in the mixed ice.

The behavior of sI CH at 135 K differs significantly from that of sII CH under the same conditions (Figure 5a). At 135 K, the IR peak at 1035 cm^{-1}, corresponding to sI CH, initially increased for the first 4 h, indicating CH formation. Subsequently, the peak gradually diminishes, reflecting slow dissociation, although a significant amount of CH still persists even after 17 h. Notably, the crystalline TMO peak at 1026 cm^{-1} decreases steadily over time. However, complete desorption is not observed here, even after 17 h, as shown in the ring puckering mode region. The O−H stretching region reveals that with time, water ice becomes increasingly ordered and compact, yet it does not crystallize. After 17 h, the intensity of the O−H band increases slightly, and desorption from the matrix begins, but water does not crystallize. This result contrasts with an isothermal RAIR study of pure

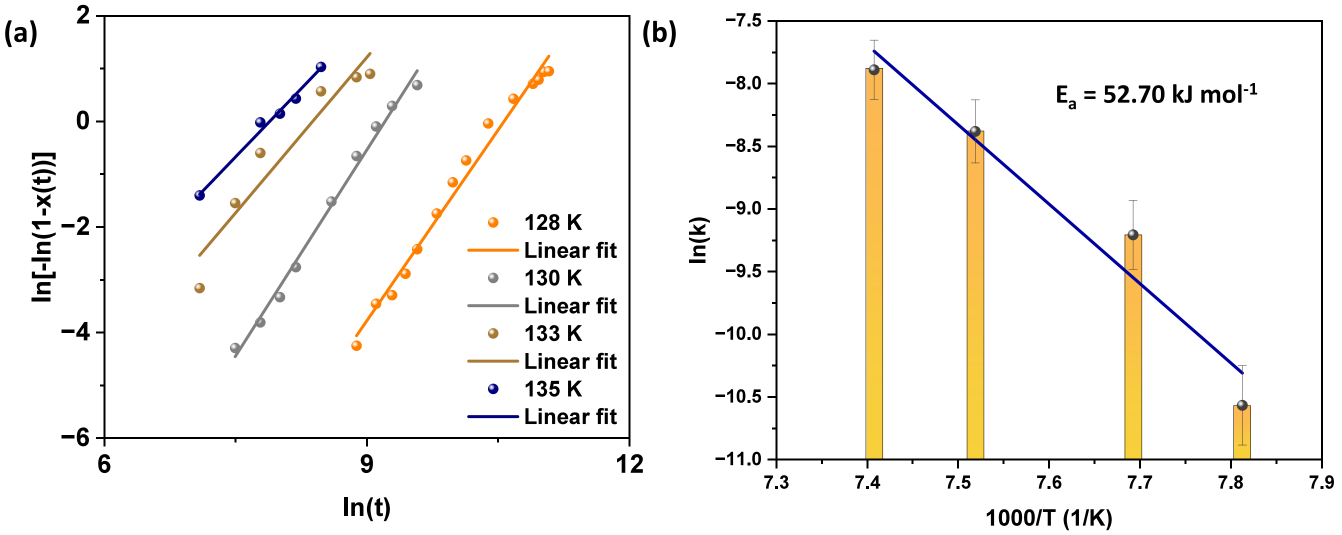

Figure 6. (a) Linear plot of the Avrami equation for ASW crystallization. Plots of $\ln(-\ln - [1 - x])$ versus $\ln(t)$ at 128, 130, 133, and 135 K were evaluated using the O−H stretching modes. The obtained data points were fitted using the Avrami equation. (b) Arrhenius plot of ln k versus $1/T$, obtained from the analysis of the slope and intercept of the linearly fitted lines of plot (a) for different temperatures. The activation energy (E_a) of ice crystallization was calculated from the slope of the linearly fitted straight line of plot (b).

amorphous water ice at 135 K, where it crystallizes to hexagonal ice in 12 h at 135 K (Figure S8). However, in the presence of sI CH, even after 17 h, water remains in a more ordered state but retains its amorphous nature. Despite the dissociation of sI CH, the anticipated crystallization of water does not occur within the experimental time scale, indicating a significant suppression of crystallization kinetics following the dissociation of sI CH compared to that of pure amorphous water ice. This might be attributed to the TMO-H_2O hydrogen bonding interaction from residual TMO in ASW for sI CH inhibiting crystallization. In sII CH, TMO completely desorbs, and ASW crystallizes in the absence of TMO-H_2O hydrogen bonding. Although this TMO-H_2O hydrogen bonding continuously diminishes as 80% of TMO desorbs within 2 h at 135 K, for sI CH. As a result, while concentration effects are certainly relevant, they do not fully explain the qualitative difference in the behavior of ASW crystallization following sI vs sII CH dissociation observed in our study, highlighting the impact of the sI CH structure in impeding phase transition.

These contrasting effects of the two CH structures of the same TMO guest molecules, namely, sI and sII, in determining the crystallization kinetics of water ice have never been observed hitherto. These differences can be attributed to structural variations between sI and sII CHs, as well as the orientation of TMO and its hydrogen bonding interactions inside the cages. While the crystallization of amorphous water ice following CH dissociation has been well-documented for both sI and sII CHs, in the case of TMO-CH, it is structure-dependent with only sII TMO-CH dissociating to form crystalline ice. Previous reports show that water transforms from amorphous ice to crystalline ice via the dissociation of CO_2 CH (sI) and DME CH (sII), suggesting that dissociation-induced crystallization is generally independent of CH structure.[3,36] This crystallization process occurs through the rapid reorientation of water molecules as they transition from the disordered amorphous phase to the more ordered crystalline phase. When dissociation is initiated at a higher temperature, a significant amount of cages break, releasing the guest molecules within a very short time window. As the hydrogen bonding network of caged water is disrupted, other water molecules in their proximity get reoriented. This combined effect of caged water and the guest molecule mobilizes water, leading to crystallization. Since sI CH is more stable, it dissociates slowly at 135 K, as observed in our study. This gradual dissociation leads to the formation of compact ice but is insufficient to induce crystallization. Additionally, TMO weakly interacts with caged water via hydrogen bonding in sI CH, a feature absent in sII CH. This hydrogen-bonded TMO may restrict caged water from interacting with amorphous ice, further hindering crystallization. As a result, crystallization at 135 K becomes even slower than that of pure water ice, possibly attributed to the stability and host−guest hydrogen bonding interaction in sI CH.

The crystallization kinetics study on the transition from CH to hexagonal ice possesses significant relevance in various scientific fields, including CH chemistry, physical chemistry, astrochemistry, atmospheric chemistry, and planetary science.[37−40] To evaluate the kinetic parameters governing this phase transition, we conducted isothermal time-dependent RAIRS experiments using a 300 ML TMO-H_2O (1:30) film within the temperature range of 128−135 K.

Figure S6 represents time-dependent RAIR spectra in the O−H stretching region at 128, 130, 133, and 135 K. In Figure S6a, the initial spectrum (0 min) displays contributions from water molecules involved in the CH phase, along with remaining ASW. After 80 min, the spectrum reveals the characteristic features of hexagonal crystalline ice, consistent with previous literature (Figure S6a).[33,35,41,42] It is well-known that pure amorphous ice converts to hexagonal ice at elevated temperatures in UHV. To validate this, we formed hexagonal ice from pure amorphous water at 135 K and compared the results to our data (Figure S8). The crystallization fraction at different temperatures versus time is shown in Figure S7 (derived from the RAIR spectra shown in Figure S6). The absorbance intensity at 3260 cm^{-1} was used to obtain the crystallization fraction, $x(t)$, by using eq 1.

Table 1. Parameters Estimated Using the Avrami Equation at Various Temperatures

temperature	128 K	130 K	133 K	135 K
n	2.41	2.60	1.96	1.72
rate constant (ks^{-1})	0.26×10^{-4}	1.00×10^{-4}	2.29×10^{-4}	3.75×10^{-4}

$$x(t) = \frac{\Delta A(1)}{\Delta A(2)} \tag{1}$$

$\Delta A(1)$ represents the difference between absorbance at a specific time t and one at time 0, and $\Delta A(2)$ is the corresponding difference in absorbance of a completely crystallized film and that at time 0. The thermodynamics of the dissociation of CH and its impact on the crystallization of water ice can be understood from the crystallization fraction. The transition of the shape of the curve from sigmoidal (occurring at a lower temperature, 128 K) to exponential (evident at a higher temperature, 135 K) (shown in Figure S6) implies a notable increase in the crystallization kinetics with temperature.

The kinetics parameters and activation energy for the CH to hexagonal ice transition were calculated using the Avrami equation.[43,44]

$$x(t) = 1 - \exp(-k.\ t)^{n} \tag{2}$$

where k is the rate constant, t is the time, and n is a parameter related to the crystallization mechanism.[44] The variable "n" can take values in the range of 1−4, and these values are used to predict the nature of the crystallization process.[45,46] Eq 2 can be rearranged in a linear form.

$$\ln(-\ln[1 - x(t)]) = n\ln(t) + n\ln k \tag{3}$$

Figure 6a shows the plots of $\ln(-\ln[1 - x(t)])$ versus $\ln(t)$ at different temperatures. The values of n and k at different temperatures were obtained using the slope and intercept of linearly fitted lines as shown in Table 1. The value calculated for n is found to be between 1.7 and 2.4, indicating that the nucleation originates from CH and ASW interfaces and progresses in a polyhedral growth pattern within the ice matrix.[4,43] The slope of the linearly fitted line of the Arrhenius plot (Figure 6b) was used to determine the activation energy (E_a) of ice crystallization. The calculated value of E_a for the phase transition from ASW to hexagonal ice is 52.70 kJ mol^{-1}. This aligns with our previous studies, which reported an activation energy of ~52−58 kJ mol^{-1} for desorption-induced ASW-to-hexagonal ice transition. This suggests that the dissociation of TMO sII CH leads to the facile crystallization of amorphous water ice to hexagonal ice.

CONCLUSIONS

In this work, we succeeded in forming TMO CHs from TMO-H_2O mixed ice under UHV, analogous to interstellar conditions. We have shown that two types of CH structures were formed at different compositions in cryogenic ices within UHV under the same temperature and pressure conditions. The 1:3 ratio of the TMO-H_2O ice mixture leads to sI CH, whereas the 1:15 ratio leads to sII CH. DFT analysis shows the presence of host−guest hydrogen bonding and structurally distorted planar TMO in sI CH, which does not occur in sII CH. While sI CH dissociation does not induce crystallization of ASW, dissociation of sII CH leads to the crystallization of ASW to hexagonal ice. The results suggest that by dissociating a specific structure of CH, the transformation of amorphous water ice to crystalline hexagonal ice can be controlled. The crystallization process accelerates as sII CH dissociates, while, on the contrary, the dissociation of sI CH retards crystallization, slower than that of pure water ice at the same temperature. Our results provide evidence that the same guest molecule creates two different CH and consequently affects ice crystallization differently at two distinct compositions. These observations describe the importance of structural conformers of enclathrated molecules in deciding the phase transition of water ice. This study also suggests the possibility of isolation of structurally hindered conformers in interstellar ices and CHs, contributing to the phase evolution of mixed molecular solids.

ASSOCIATED CONTENT

Supporting Information

The Supporting Information is available free of charge at https://pubs.acs.org/doi/10.1021/acs.jpcc.5c01603.

Temperature and time-dependent RAIR spectra of pure TMO and TMO-H_2O ice mixtures (PDF)

AUTHOR INFORMATION

Corresponding Author

Thalappil Pradeep − *DST Unit of Nanoscience (DST UNS) and Thematic Unit of Excellence (TUE), Department of Chemistry, Indian Institute of Technology Madras, Chennai 600036, India; International Centre for Clean Water, IIT Madras Research Park, Chennai 600113, India;* orcid.org/0000-0003-3174-534X; Email: pradeep@iitm.ac.in

Authors

Soham Chowdhury − *DST Unit of Nanoscience (DST UNS) and Thematic Unit of Excellence (TUE), Department of Chemistry, Indian Institute of Technology Madras, Chennai 600036, India*

Bijesh K. Malla − *DST Unit of Nanoscience (DST UNS) and Thematic Unit of Excellence (TUE), Department of Chemistry, Indian Institute of Technology Madras, Chennai 600036, India*

Gaurav Vishwakarma − *DST Unit of Nanoscience (DST UNS) and Thematic Unit of Excellence (TUE), Department of Chemistry, Indian Institute of Technology Madras, Chennai 600036, India;* orcid.org/0009-0002-6076-3299

Anupriya Nyayban − *DST Unit of Nanoscience (DST UNS) and Thematic Unit of Excellence (TUE), Department of Chemistry, Indian Institute of Technology Madras, Chennai 600036, India*

Complete contact information is available at: https://pubs.acs.org/10.1021/acs.jpcc.5c01603

Author Contributions

T.P. and S.C. designed the experiments, S.C. and B.K.M. performed the experiments, and S.C., B.K.M., and G.V. analyzed the results. T.P. proposed the project and supervised the progress. A.N. performed the quantum chemical calculations. The manuscript was written with the contributions of all authors.

Notes

The authors declare no competing financial interest.

■ ACKNOWLEDGMENTS

We acknowledge the Science and Engineering Research Board (SERB), Department of Science and Technology (DST), Government of India, for research funding through a CRG grant (CRG/2018/003922) and a Swarnajayanti fellowship. T.P. acknowledges funding from the Centre of Excellence on Molecular Materials and Functions under the Institution of Eminence scheme of IIT Madras. S.C., G.V., and A.N. thank IITM for their research fellowship. B.K.M. thanks the Council of Scientific and Industrial Research (CSIR) for his research fellowship.

■ REFERENCES

(1) Ghosh, J.; Vishwakarma, G.; Kumar, R.; Pradeep, T. Formation and Transformation of Clathrate Hydrates under Interstellar Conditions. *Acc. Chem. Res.* **2023**, *56* (16), 2241−2252.

(2) Malla, B. K.; Vishwakarma, G.; Chowdhury, S.; Selvarajan, P.; Pradeep, T. Formation of Ethane Clathrate Hydrate in Ultrahigh Vacuum by Thermal Annealing. *J. Phys. Chem. C* **2022**, *126* (42), 17983−17989.

(3) Malla, B. K.; Vishwakarma, G.; Chowdhury, S.; Nayak, S. K.; Yamijala, S. S. R. K. C.; Pradeep, T. Formation and Dissociation of Dimethyl Ether Clathrate Hydrate in Interstellar Ice Mimics. *J. Phys. Chem. C* **2024**, *128* (6), 2463−2470.

(4) Vishwakarma, G.; Malla, B. K.; Chowdhury, S.; Khandare, S. P.; Pradeep, T. Existence of Acetaldehyde Clathrate Hydrate and Its Dissociation Leading to Cubic Ice under Ultrahigh Vacuum and Cryogenic Conditions. *J. Phys. Chem. Lett.* **2023**, *14* (23), 5328−5334.

(5) Vishwakarma, G.; Malla, B. K.; Reddy, K. S. S. V. P.; Ghosh, J.; Chowdhury, S.; Yamijala, S. S. R. K. C.; Reddy, S. K.; Kumar, R.; Pradeep, T. Induced Migration of CO2 from Hydrate Cages to Amorphous Solid Water under Ultrahigh Vacuum and Cryogenic Conditions. *J. Phys. Chem. Lett.* **2023**, 2823−2829.

(6) Tychengulova, A.; Katpayeva, K.; Shomshekova, S.; Ibragimova, S.; Golikov, O.; Yerezhep, D.; Sokolov, D.; Aldiyarov, A. Laboratory Studies of the Clathrate Hydrate Formation in the Carbon Dioxide-Water Mixtures at Interstellar Conditions. *ACS Omega* **2025**, *10*, 1237−1248.

(7) Malla, B. K.; Yang, D.-S.; Pradeep, T. Growth of Clathrate Hydrates in Nanoscale Ice Films Observed Using Electron Diffraction and Infrared Spectroscopy. *J. Phys. Chem. Lett.* **2025**, *16*, 365−371.

(8) *Molecules [CDMS classic documentation]*. https://cdms.astro.uni-koeln.de/classic/molecules (accessed January 2025).

(9) Puzzarini, C.; Alessandrini, S. Interstellar Ices: A Factory of the Origin-of-Life Molecules. *ACS Cent. Sci.* **2024**, *10* (1), 13−15.

(10) Blake, D.; Allamandola, L.; Sandford, S.; Hudgins, D.; Freund, F. Clathrate Hydrate Formation in Amorphous Cometary Ice Analogs in Vacuo. *Science* **1979**, *254* (5031), 548−551.

(11) Sloan, E. D. Fundamental Principles and Applications of Natural Gas Hydrates. *Nature 2003 426:6964* **2003**, *426* (6964), 353−359. .

(12) Yeon, S. H.; Seol, J.; Lee, H. Structure Transition and Swapping Pattern of Clathrate Hydrates Driven by External Guest Molecules. *J. Am. Chem. Soc.* **2006**, *128* (38), 12388−12389.

(13) Halpern, Y.; Thieu, V.; Henning, R. W.; Wang, X.; Schultz, A. J. Time-Resolved in Situ Neutron Diffraction Studies of Gas Hydrate: Transformation of Structure II (SII) to Structure I (SI). *J. Am. Chem. Soc.* **2001**, *123* (51), 12826−12831.

(14) Devlin, J. P. Structure, Spectra, and Mobility of Low-Pressure Ices: Ice I, Amorphous Solid Water, and Clathrate Hydrates at T < 150 K. *J. Geophys Res. Planets* **2001**, *106* (E12), 33333−33349.

(15) McGuire, B. A.; Carroll, P. B.; Loomis, R. A.; Finneran, I. A.; Jewell, P. R.; Remijan, A. J.; Blake, G. A. Discovery of the Interstellar Chiral Molecule Propylene Oxide (CH3CHCH2O). *Science* **2016**, *352* (6292), 1449−1452.

(16) Ghosh, J.; Bhuin, R. G.; Ragupathy, G.; Pradeep, T. Spontaneous Formation of Tetrahydrofuran Hydrate in Ultrahigh Vacuum. *J. Phys. Chem. C* **2019**, *123* (26), 16300−16307.

(17) Udachin, K. A.; Ratcliffe, C. I.; Ripmeester, J. A. Structure, Dynamics and Ordering in Structure I Ether Clathrate Hydrates from Single-Crystal X-Ray Diffraction And2H NMR Spectroscopy. *J. Phys. Chem. B* **2007**, *111* (39), 11366−11372.

(18) Maşlakcı, Z.; Devlin, J. P.; Uras-Aytemiz, N. H-Bonding Behavior of Ethylene Oxide within the Clathrate Hydrates Revisited: Experiment and Theory. *Chem. Phys. Lett.* **2020**, *754*, No. 137728.

(19) Buch, V.; Devlin, J. P.; Monreal, I. A.; Jagoda-Cwiklik, B.; Uras-Aytemiz, N.; Cwiklik, L. Clathrate Hydrates with Hydrogen-Bonding Guests. *Phys. Chem. Chem. Phys.* **2009**, *11* (44), 10245−10265.

(20) Fleyfel, F.; Devlin, J. P. Infrared Spectra of Large Clusters Containing Small Ether Molecules: Liquid, Crystalline, and Clathrate-hydrate Cluster Spectra. *J. Chem. Phys.* **1998**, *92* (1), 36.

(21) Subramaniam, S.; Lance, M. J.; Rawn, C. J.; Chakoumakos, B. C.; Rondinone, A. J. Raman Spectroscopic Studies on Structure I and Structure IItrimethylene Oxide Hydrate. *Canadian J. Phys.* **2005**, *83* (9), 941−949.

(22) Rondinone, A. J.; Chakoumakos, B. C.; Rawn, C. J.; Ishii, Y. Neutron Diffraction Study of Structure I and Structure II Trimethylene Oxide Clathrate Deuterate. *J. Phys. Chem. B* **2003**, *107* (25), 6046−6050.

(23) Bag, S.; Bhuin, R. G.; Methikkalam, R. R. J.; Pradeep, T.; Kephart, L.; Walker, J.; Kuchta, K.; Martin, D.; Wei, J. Development of Ultralow Energy (1−10 EV) Ion Scattering Spectrometry Coupled with Reflection Absorption Infrared Spectroscopy and Temperature Programmed Desorption for the Investigation of Molecular Solids. *Rev. Sci. Instrum.* **2014**, *85* (1). .

(24) Malla, B. K.; Vishwakarma, G.; Chowdhury, S.; Pradeep, T. Vacuum Ultraviolet Photolysis of Condensed Methyl Chloride in Interstellar Model Conditions and Trapping of Intermediates at Intergrain Interfaces. *J. Phys. Chem. C* **2023**, *127* (50), 24149−24157.

(25) Malla, B. K.; Chowdhury, S.; Paliwal, D.; Hanoona, K. M.; Vishwakarma, G.; Methikkalam, R. R. J.; Pradeep, T. Simulated Interstellar Photolysis of N2O Ice: Selectivity in Photoproducts. *J. Phys. Chem. C* **2025**, *129*, 1120−1128.

(26) Moon, E. S.; Kang, H.; Oba, Y.; Watanabe, N.; Kouchi, A. DIRECT EVIDENCE FOR AMMONIUM ION FORMATION IN ICE THROUGH ULTRAVIOLET-INDUCED ACID−BASE REACTION OF NH3 WITH H3O+. *Astrophys. J.* **2010**, *713* (2), 906.

(27) Bartmess, J. E.; Georgiadis, R. M. Empirical Methods for Determination of Ionization Gauge Relative Sensitivities for Different Gases. *Vacuum* **1983**, *33* (3), 149−153.

(28) Mizuno, K.; Masuda, Y.; Yamamura, T.; Kitamura, J.; Ogata, H.; Bako, I.; Tamai, Y.; Yagasaki, T. Roles of the Ether Oxygen in Hydration of Tetrahydrofuran Studied by IR, NMR, and DFT Calculation Methods. *J. Phys. Chem. B* **2009**, *113* (4), 906−915.

(29) Mohammadi-Manesh, H.; Ghafari, H.; Alavi, S. Molecular Dynamics Study of Guest-Host Hydrogen Bonding in Ethylene Oxide, Trimethylene Oxide, and Formaldehyde Structure i Clathrate Hydrates. *J. Phys. Chem. C* **2017**, *121* (16), 8832−8840.

(30) Sloan, E. D., Jr.; Koh, C. A.; Koh, C. A. Clathrate Hydrates of Natural Gases. *Clathrate Hydrates of Natural Gases* **2007**.

(31) Monreal, I. A.; Cwiklik, L.; Jagoda-Cwiklik, B.; Devlin, J. P. Classical to Nonclassical Transition of Ether-HCN Clathrate Hydrates at Low Temperature. *J. Phys. Chem. Lett.* **2010**, *1* (1), 290−294.

(32) Monreal, I. A.; Devlin, J. P.; Maşlakc, Z.; Çiçek, M. B.; Uras-Aytemiz, N. Controlling Nonclassical Content of Clathrate Hydrates through the Choice of Molecular Guests and Temperature. *J. Phys. Chem. A* **2011**, *115* (23), 5822−5832.

(33) Ghosh, J.; Vishwakarma, G.; Das, S.; Pradeep, T. Facile Crystallization of Ice Ihvia Formaldehyde Hydrate in Ultrahigh

Vacuum under Cryogenic Conditions. *J. Phys. Chem. C* **2021**, *125* (8), 4532−4539.

(34) Ghosh, J.; Bhuin, R. G.; Vishwakarma, G.; Pradeep, T. Formation of Cubic Ice via Clathrate Hydrate, Prepared in Ultrahigh Vacuum under Cryogenic Conditions. *J. Phys. Chem. Lett.* **2020**, *11* (1), 26−32.

(35) Vishwakarma, G.; Ghosh, J.; Pradeep, T. Desorption-Induced Evolution of Cubic and Hexagonal Ices in an Ultrahigh Vacuum and Cryogenic Temperatures. *Phys. Chem. Chem. Phys.* **2021**, *23* (41), 24052−24060.

(36) Falenty, A.; Hansen, T. C.; Kuhs, W. F.; Hansen, T. C. *Cubic Ice Formation and Annealing during CO2 Clathrate Hydrate Decomposition at Low Temperatures Cubic Ice Formation and Annealing during CO 2 Clathrate Hydrate Decomposition at Low Temperatures*; Hokkaido University Press, 2011.

(37) Cao, H. S. Formation and Crystallization of Low-Density Amorphous Ice. *J. Phys. D Appl. Phys.* **2021**, *54* (20), 203002.

(38) Takeya, S.; Fujihisa, H.; Alavi, S.; Ohmura, R. Thermally Induced Phase Transition of Cubic Structure II Hydrate: Crystal Structures of Tetrahydropyran-CO2 Binary Hydrate. *J. Phys. Chem. Lett.* **2023**, *14* (7), 1885−1891.

(39) Minissale, M.; Aikawa, Y.; Bergin, E.; Bertin, M.; Brown, W. A.; Cazaux, S.; Charnley, S. B.; Coutens, A.; Cuppen, H. M.; Guzman, V.; Linnartz, H.; McCoustra, M. R. S.; Rimola, A.; Schrauwen, J. G. M.; Toubin, C.; Ugliengo, P.; Watanabe, N.; Wakelam, V.; Dulieu, F. Thermal Desorption of Interstellar Ices: A Review on the Controlling Parameters and Their Implications from Snowlines to Chemical Complexity. *ACS Earth Space Chem.* **2022**, *6* (3), 597−630.

(40) Bartels-Rausch, T.; Bergeron, V.; Cartwright, J. H. E.; Escribano, R.; Finney, J. L.; Grothe, H.; Gutiérrez, P. J.; Haapala, J.; Kuhs, W. F.; Pettersson, J. B. C.; Price, S. D.; Sainz-Díaz, C. I.; Stokes, D. J.; Strazzulla, G.; Thomson, E. S.; Trinks, H.; Uras-Aytemiz, N. Ice Structures, Patterns, and Processes: A View across the Icefields. *Rev. Mod. Phys.* **2012**, *84* (2), 885−944.

(41) Vishwakarma, G.; Malla, B. K.; Methikkalam, R. R. J.; Pradeep, T. Rapid Crystallization of Amorphous Solid Water by Porosity Induction. *Phys. Chem. Chem. Phys.* **2022**, *24* (42), 26200−26210.

(42) Watanabe, N.; Kouchi, A. Ice Surface Reactions: A Key to Chemical Evolution in Space. *Prog. Surf. Sci.* **2008**, *83* (10−12), 439−489.

(43) Avrami, M. Kinetics of Phase Change. II Transformation-Time Relations for Random Distribution of Nuclei. *J. Chem. Phys.* **1940**, *8* (2), 212−224.

(44) Harada, K.; Sugimoto, T.; Kato, F.; Watanabe, K.; Matsumoto, Y. Thickness Dependent Homogeneous Crystallization of Ultrathin Amorphous Solid Water Films. *Phys. Chem. Chem. Phys.* **2020**, *22* (4), 1963−1973.

(45) Hage, W.; Hallbrucker, A.; Mayer, E.; Johari, G. P. Crystallization Kinetics of Water below 150 K. *J. Chem. Phys.* **1998**, *100* (4), 2743.

(46) Lee, D. H.; Kang, H. Acid-Promoted Crystallization of Amorphous Solid Water. *J. Phys. Chem. C* **2018**, *122* (42), 24164−24170.

https://doi.org/10.1021/acs.jpcc.5c01603
J. Phys. Chem. C 2025, 129, 8937−8945